W.D. Goodhue

Using Molecular-Beam Epitaxy to Fabricate Quantum-Well Devices

Recent advances in thin-film crystal-growth techniques such as molecular-beam epitaxy (MBE) have enabled the fabrication of quantum-well devices, which consist of alternating layers of various crystalline solid materials so thin that the materials' combined quantum-mechanical properties override their individual bulk properties. By using MBE, we constructed a number of quantum-well devices that have applications in ultrahigh-speed analog, digital, and electro-optical integrated and hybrid systems.

Scientists discovered the basic principles of quantum mechanics more than half a century ago. Only recently, however, have researchers been able to fabricate devices that exploit the quantum-mechanical behavior of carriers in epitaxially grown ultrathin semiconductor layers. These devices couple many basic quantum-mechanical principles with recent advances in the control of the doping, the thicknesses, and the bandgaps of epitaxial semiconductor layers. Although bulk-semiconductor technologies use a few micrometers of a wafer's thickness to form devices, quantum-well technology sometimes requires as little as 7 nm or less. Attaining such minuscule geometries was impossible until the recent development of thin-film semiconductor crystal-growth techniques such as molecular-beam epitaxy (MBE).

MBE is an ultrahigh-vacuum epitaxial-growth technology. In MBE, molecular beams of specific materials impinge upon an appropriately prepared wafer placed in an ultrahigh-vacuum environment. The reaction results in the growth of a thin epitaxial film on the wafer's surface. By manipulating the arrival rates of the beams and the temperature of the wafer surface, the process can be controlled so that layers of specified materials are grown to atomic-layer thicknesses, which makes the process suitable for quantum-well device engineering.

This article will briefly review some of the basic principles underlying quantum-well semiconductors, discuss the use of MBE to fabricate GaAs/$Al_xGa_{1-x}As$ semiconductor materials, and describe several quantum-well devices that have been developed with MBE at Lincoln Laboratory.

(*Editor's note: Readers who wish to learn in more detail about quantum-well devices, bandgap engineering, and modern thin-film crystal-growth techniques can find excellent review articles in Refs. 1–6.*)

Semiconductor Quantum-Wells

The energy bands of semiconductors are complicated. Figure 1 shows the band diagram of GaAs. The point of lowest energy in the conduction band is called the conduction-band edge, and the point of highest energy in the valence band is called the valence-band edge. The energy difference of these two points is the semiconductor's bandgap, denoted as E_{gap} in Fig. 1.

If the two band-edge points occur at the same lattice-momentum value, the gap is a direct gap. Otherwise, it is an indirect gap. From Fig. 1 we see that GaAs is a direct-gap semiconductor. Silicon and AlAs, on the other hand, are indirect-gap semiconductors.

The band structures of compound semiconductors can vary with the relative concentration of constituent elements. For example, indirect-gap AlAs can be mixed with direct-gap GaAs to form an alloy $Al_xGa_{1-x}As$, which has a direct gap only when $x < 0.43$. Figure 2 diagrams the

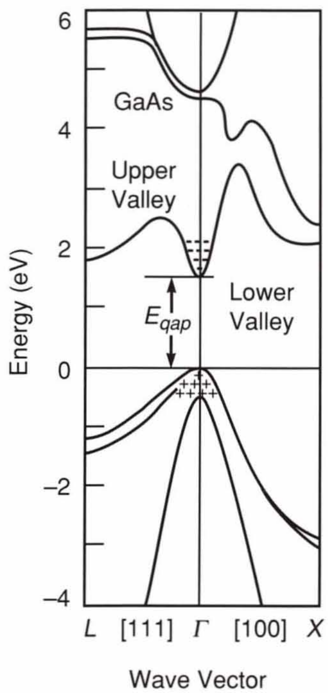

Fig. 1—Band diagram for GaAs. (After Sze, Ref. 5.) E_{gap} *is the energy bandgap. Plus (+) signs indicate holes in the valence bands and minus (–) signs indicate electrons in the conduction bands.*

bandgap and lattice constant of a variety of semiconductor compounds comprising elements from Groups III and V of the periodic table.

GaAs/$Al_xGa_{1-x}As$ materials are unique among III-V semiconductors because the dimensions of the crystalline lattice of GaAs and $Al_xGa_{1-x}As$ match within 1% for all values of x, yet the difference in bandgaps of the two materials can vary at room temperature from 0 eV to as much as 0.75 eV (as x increases from 0 to 1). The first property makes heteroepitaxy straightforward; the second property makes fabrication of quantum wells possible.

A quantum well is formed when sandwiching a thin layer of material between two layers of a compatible material causes the energy bands of the composite material to form an energy minimum in the conduction and/or valence band of the thin sandwiched layer. Consequently, the electrons and/or holes in the thin layer are confined in such a manner that they behave quantum mechanically as particles in a box with discrete, bound energy states.

Figure 3 shows the alignment of the conduction- and valence-band edges of two types of heterojunctions. We will focus on the $Al_xGa_{1-x}As$ to GaAs heterojunction (Fig. 3[a]). The Γ-valley conduction band offset between these materials is about 65% of the total bandgap difference, which makes the valence band offset about 35%. (The Γ-valley is the lowest point in the conduction bands of GaAs and $Al_xGa_{1-x}As$ when $x \leq 0.43$.) Other alignments, such as the staggered alignment shown in Fig. 3(b), are possible when other semiconductors are used. The GaAs-$Al_xGa_{1-x}As$ system is referred to as a type I system.

Stacking alternating layers of various concentrations of $Al_xGa_{1-x}As$ makes it possible to fabricate materials with unusual synthetic band structures. Figure 4 shows several possibilities. In fact, by alternating very thin layers of materials such as GaAs and AlAs, one can construct a *superlattice* material (Fig. 4[e]), which is unlike

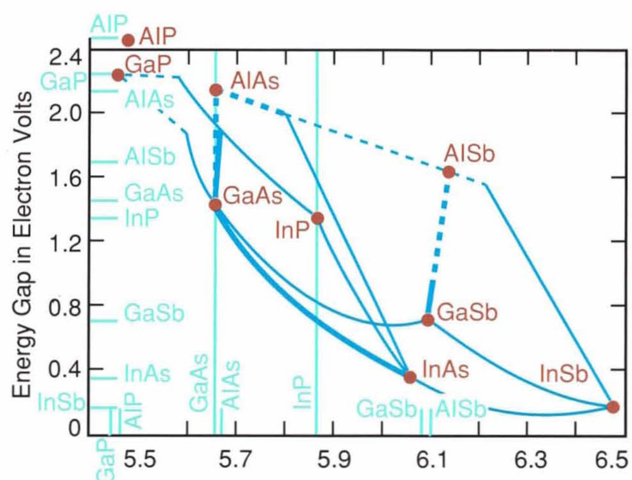

Fig. 2—Bandgap versus lattice constant for a variety of III-V semiconductor compounds. (After Cho, Ref. 2.) Note that GaAs is lattice-matched to AlAs, which simplifies the problems associated with growing epitaxial layers of the two materials. However, heteroepitaxy of non-lattice-matched materials such as AlAs and $In_{0.2}Ga_{0.8}As$ *is also possible because the lattice constants of these two materials are around 5.7 to 5.8 Å and the structures under discussion have dimensions of 70 to 1,000 Å.*

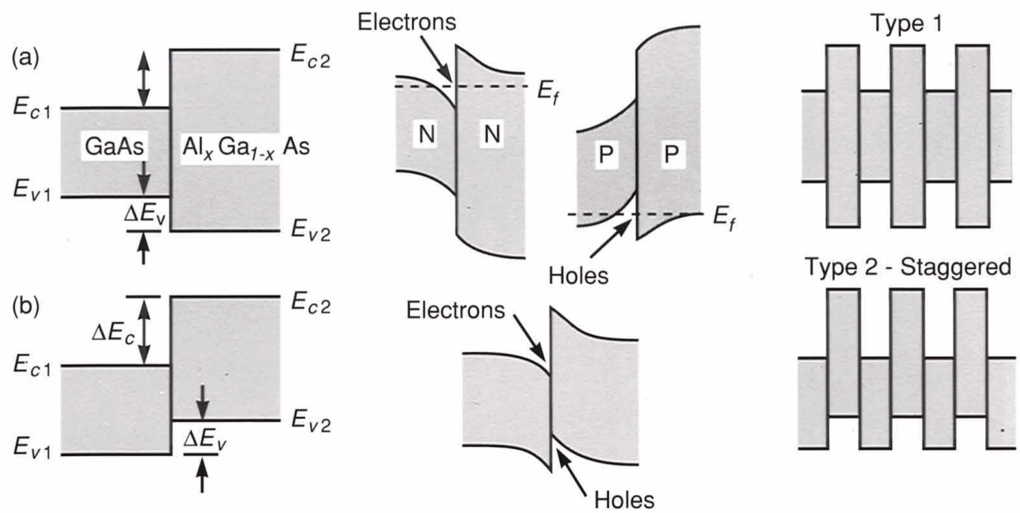

Fig. 3—Discontinuities of band-edge energies at two kinds of heterointerfaces: band offsets (left column), band bending and carrier confinement (middle column), and superlattices (right column). (After Esaki, Ref. 3, p. 1613.) Copyright © 1986, IEEE.

either of its constituent semiconductors.

Both the conduction- and valence-band portions of Fig. 4(a) are the semiconductor analogs of the classic quantum-mechanical problem of a particle in a one-dimensional box. Consequently, the conduction and valence bands can be analyzed exactly as in elementary physics. The particle can be either a heavy or light hole with effective mass m_{hh}^* or m_{lh}^*, or an electron with effective mass m_e^*. When the potential well is sufficiently thin, the particle inside behaves quantum mechanically; i.e., the particle exhibits discrete energy levels. The semiconductor system is referred to as a quantum well. In the other two dimensions, the particle behaves with a continuum of energy levels as dictated by the usual band structure.

For the structure of Fig. 4(a), Fig. 5 plots several of the allowable energy states of the electrons and both types of holes as a function of well thickness within the band. Figure 5 shows that the onset of obvious quantum-mechanical effects in the GaAs/$Al_xGa_{1-x}As$ system occurs when the quantum-well thickness is below 50 nm. Figure 6 shows several bound-state wave functions of a single 12-nm-thick square quantum well.

In addition to the single square well, Fig. 4 contains more complicated structures in which additional variables allow for the engineering of wave functions with greater complexities. For the asymmetric coupled well of Fig. 4(d), Fig. 7 shows wave functions of the structure under the influence of electric fields of various strengths. From Fig. 7, we see that we can engineer the e_1 and h_2 wave functions so that when we apply a moderate electric field to the well (Fig. 7[c]), the well's e_1 and h_2 wave functions overlap, which creates a strong absorption at a photon energy equal to

$$E_{gap} + E_{h_2} + E_{e_1}.$$

If we apply either too small or too large an electric field (Fig. 7[a] and Fig. 7[e], respectively), the overlap of the wave functions is minimized, which diminishes the absorption. Thus we can use asymmetric coupled wells in electro-absorptive modulation devices [7, 8].

In the design of quantum-well devices, the properties of the single direct-bandgap square quantum well that are most easily exploited are light absorption and emission, and electron-transport properties perpendicular and parallel to the epitaxial layers. We will discuss several devices developed at Lincoln Laboratory that utilize these properties. But first we will review the MBE fabrication technology used to create structures similar to those of Fig. 4.

Fundamentals of MBE

A.Y. Cho and J.R. Arthur [2, 9] invented the MBE process in the late 1960s. The technology was used in the early 1970s to verify R. Tsu and L. Esaki's prediction [10, 11] that superlattices with interesting electron-transport properties could be fabricated. In the mid-1970s, R. Dingle [1] used MBE to fabricate some of the first layers that exhibited optical quantum-well effects. Since then, laboratories around the world have generated an enormous number of devices and papers based on MBE materials.

A typical MBE system is depicted in Fig. 8. MBE systems usually consist of three ultrahigh-vacuum chambers: an introduction chamber, a sample-preparation chamber, and a growth chamber. The introduction chamber, as the name implies, is used to enter an appropriately

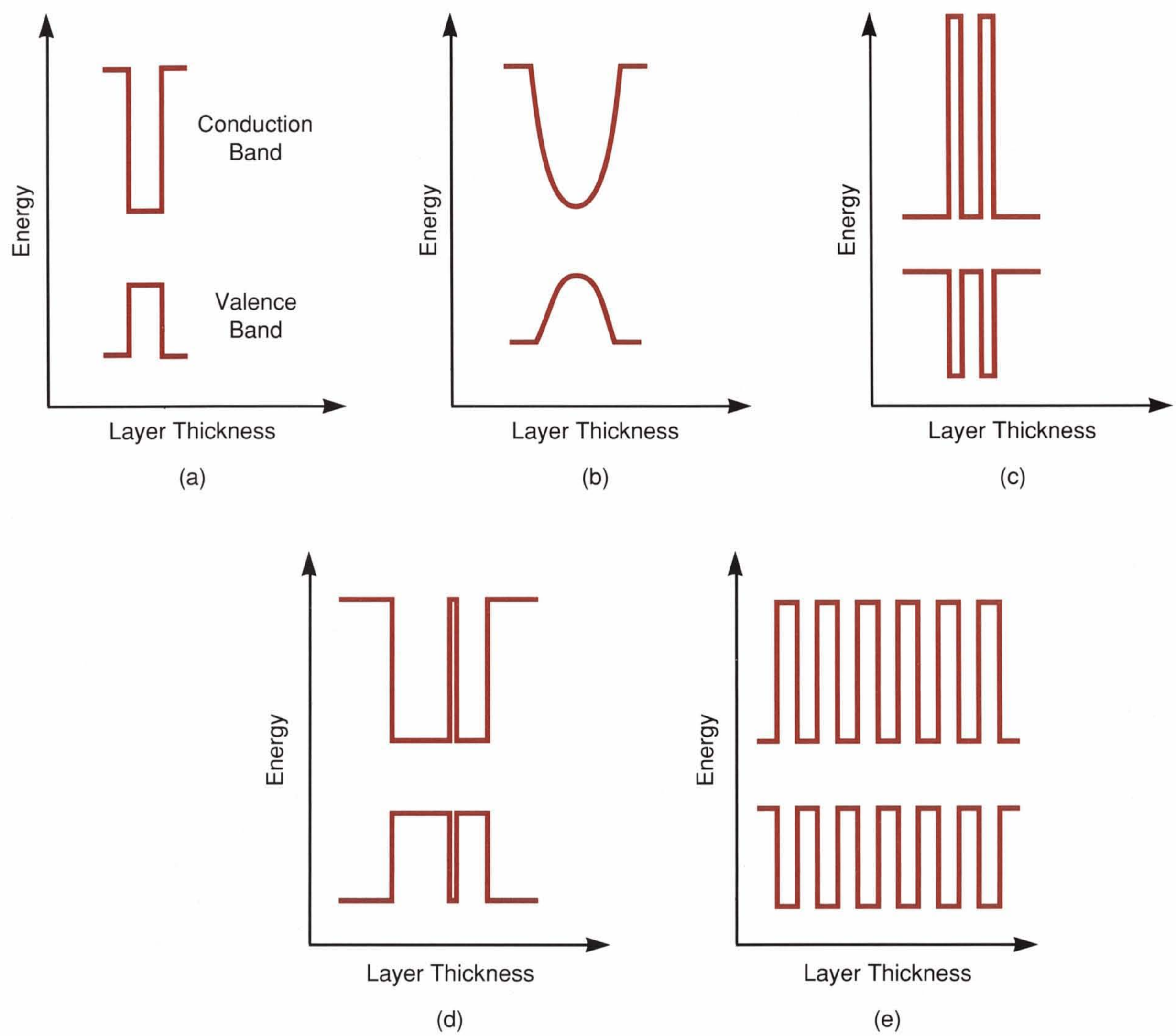

Fig. 4—Some of the possible band structures that can be created by using heteroepitaxy of GaAs and $Al_xGa_{1-x}As$. The diagrams are of (a) a square quantum well, (b) a parabolic well, (c) a double-barrier structure, (d) an asymmetric coupled quantum well, and (e) a superlattice.

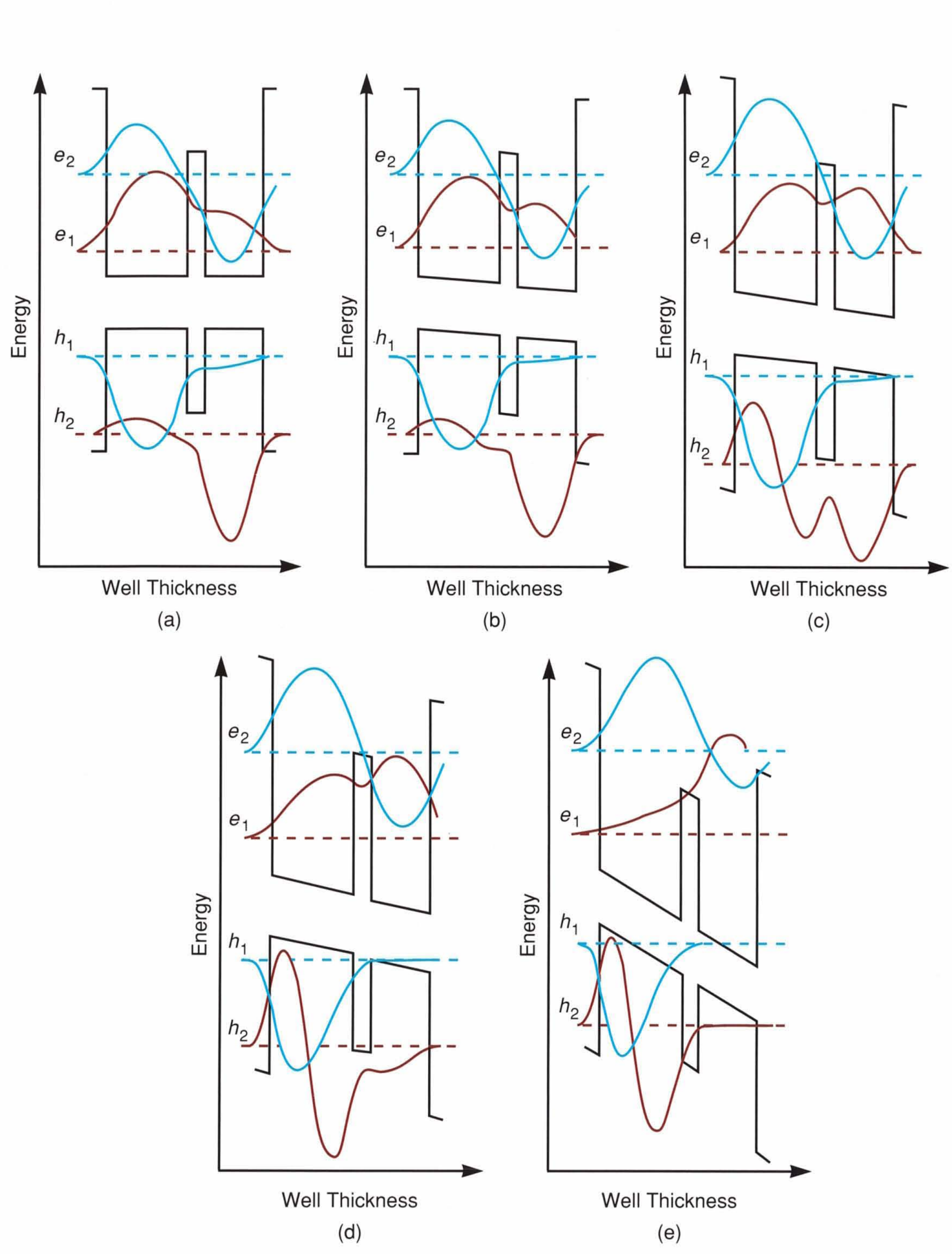

Fig. 7—Plots showing the behavior of several of the wave functions of an asymmetric coupled quantum well under the influence of an applied electric field. Here e_1 *and* e_2 *denote bound electrons while* h_1 *and* h_2 *denote bound holes. After H.Q. Le et al. in Refs. 7 and 8.*

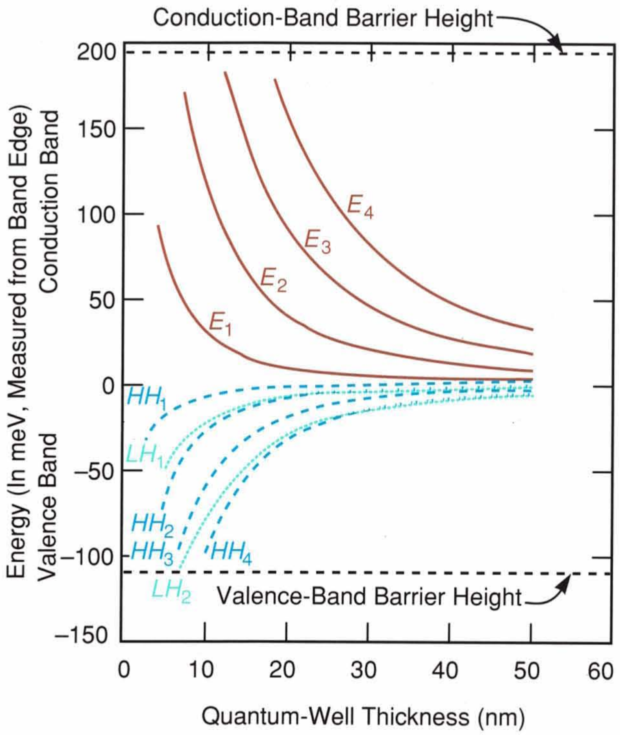

Fig. 5—Plot of the energy states of the electrons and holes of a GaAs/$Al_{0.2}Ga_{0.8}As$ quantum well as a function of well thickness. The plot assumes a finite square-well model. E_n *denotes the* n*th electron state,* LH_n *denotes the* n*th light-hole state, and* HH_n *denotes the* n*th heavy-hole state.*

prepared wafer, mounted on a molybdenum holder, into an MBE system. The preparation chamber then heats the wafer and holder to a temperature sufficiently high to drive off any atmospheric contaminants from the sample's surface. The growth chamber, with a base pressure of 10^{-11} Torr (comparable to that of intergalactic outer space), is the heart of an MBE system. In the growth chamber, samples are first rotated into a position that facilitates crystal growth. The samples are then heated to the appropriate temperature and bombarded with molecular beams of constituent and dopant materials produced by evaporating the desired elemental materials in ultraclean furnaces. By impinging the appropriate fluxes of these beams on the samples, we can initiate epitaxial single-crystal growth.

In the GaAs materials system, GaAs epitaxial layers will grow on a GaAs substrate at a rate of 1 μm/h under the following conditions: substrate surface temperature of 580°C; Ga-beam equivalent pressure of 5×10^{-7} Torr, corresponding to a Ga furnace temperature of about 1185°C; and an As-beam equivalent pressure of 5×10^{-6} Torr, corresponding to an As furnace temperature of about 310°C.

MBE systems can also add dopants such as beryllium and silicon to a growing epitaxial layer. Since so little dopant is required, the concentration is determined strictly by the growth rate of the material layers and the temperature

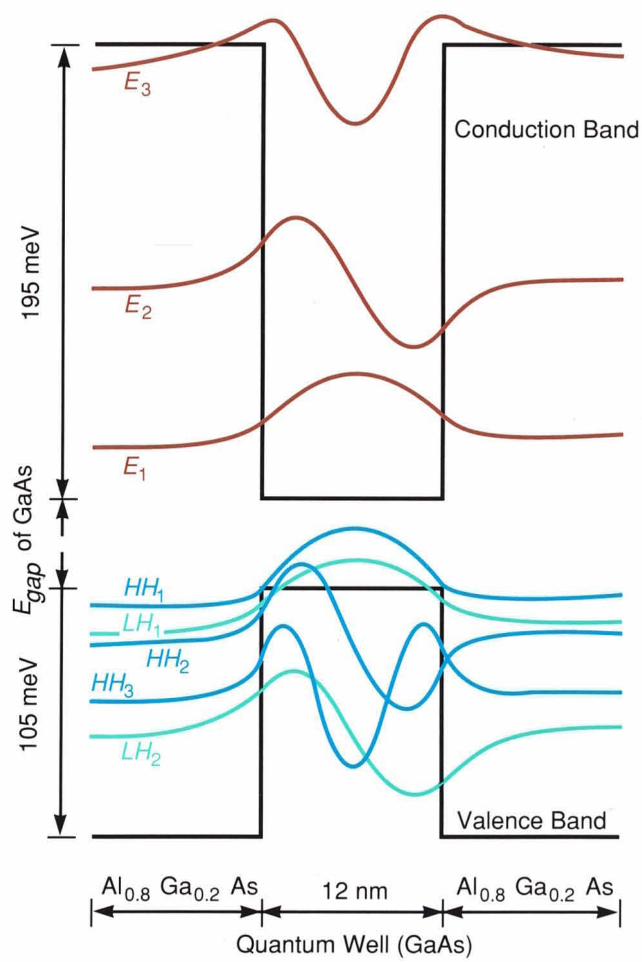

Fig. 6—Electron and hole wave functions of a 12-nm-thick square quantum well formed with GaAs and $Al_{0.2}Ga_{0.8}As$. E_n *denotes the* n*th electron state;* LH_n *denotes the* n*th light-hole state; and* HH_n *denotes the* n*th heavy-hole state.*

of the dopant furnace. For example, given the GaAs growth rate of 1 μm/h, we can achieve electron carrier concentrations ranging from 5×10^{14} to 5×10^{18} cm^{-3} by adding silicon to the growing GaAs. In this case the dopant is heated in a furnace at a temperature ranging from 1,100°C to 1,440°C. We can achieve similar hole-carrier concentrations by adding beryllium at a furnace temperature ranging from 650°C to 900°C.

With the addition of an Al furnace and by controlling the Al flux with respect to the Ga and As fluxes, we can grow the entire range of $Al_xGa_{1-x}As$ compounds, from $x = 0$ to $x = 1$. Furthermore, through the use of shutters in front of the dopant and constituent beams, we can abruptly change a material's composition or its doping. The shutters control the beams so that after a flux is turned off, no residual molecules of the beam grow on the sample's surface. Consequently, we can change the dopants and constituents within an atomic monolayer of a sample's growing surface.

Because a growth chamber's cleanliness directly affects the quality of the fabricated epitaxial layers, MBE systems incorporate many measures to limit the contamination of wafer samples. Impurities emanating from the inside walls of the chamber are minimized through chemical-passivation procedures during the chamber's fabrication and through the use of unconventional but ultraclean metals and ceramics such as titanium, tantalum, molybdenum, and pyrolytic boron nitride in the chamber's designated hot zones. If a system has to be opened later for repairs, it is subsequently baked to drive out any contaminants. In addition, during the crystal-growth process, liquid-nitrogen cryopanels assist an MBE system's ion pumps by freezing out residual CO_2, O_2, and other gases that degrade the electrical and optical properties of the growing crystal. Residual-gas mass spectrometers periodically monitor the gas constituents in the growth chamber. MBE systems are also designed to minimize wafer contamination from macroscopic particulates of flaking polycrystalline material that form on the inner walls of the growth chamber. For example, a wafer's growth surface is kept in a vertical position at all times to limit such particulate contamination.

MBE is an extremely powerful tool for growing epitaxial layers because it can control the interaction of the molecules and atoms on a wafer's growing surface. The control is interactive through the use of *in situ* reflection electron diffraction (RED), also called reflection high-energy electron diffraction. In RED, an electron beam is projected at a glancing incidence to a sample. The electron beam diffracts, emerges from the sample's surface, and produces a RED pattern. No other growth technology to date provides such immediate information about the growth of a layer on a wafer's surface.

A brief discussion of growth kinetics and the information obtained with RED is in order to understand the extent of control that this technology makes possible. We will focus on GaAs. For a variety of reasons beyond the scope of this article, the preferred orientation for MBE epitaxial growth for GaAs is the (100) orientation.

By altering the temperature and As pressure at a sample's surface, we can choose whether the last, or surface, layer will be a plane of Ga or As atoms. Dangling bonds of either type of atom attach to their neighbors to form a surface reconstruction that is periodic. In MBE, we can alter the beam fluxes and the wafer's surface temperature to control surface reconstruction and thereby to enhance desired properties of the layers during the growth process.

We observe the reconstructed surfaces with the RED process. Glancing incidence is used to enhance Bragg diffraction from only the top two or three monolayers of a crystal, i.e., the crystal's surface-reconstruction layers. The diffraction pattern, which is projected onto a phosphorus screen, consists of a number of lines. The spacing of the brightest lines is directly related to the number and spacing of the crystal planes; the spacing of the weaker lines between the stronger lines is directly related to the periodicity of the surface reconstruction.

Figures 9(a), 9(b), and 9(c), respectively, show the patterns generated by a gallium-rich, a gallium-stabilized, and an arsenic-stabilized

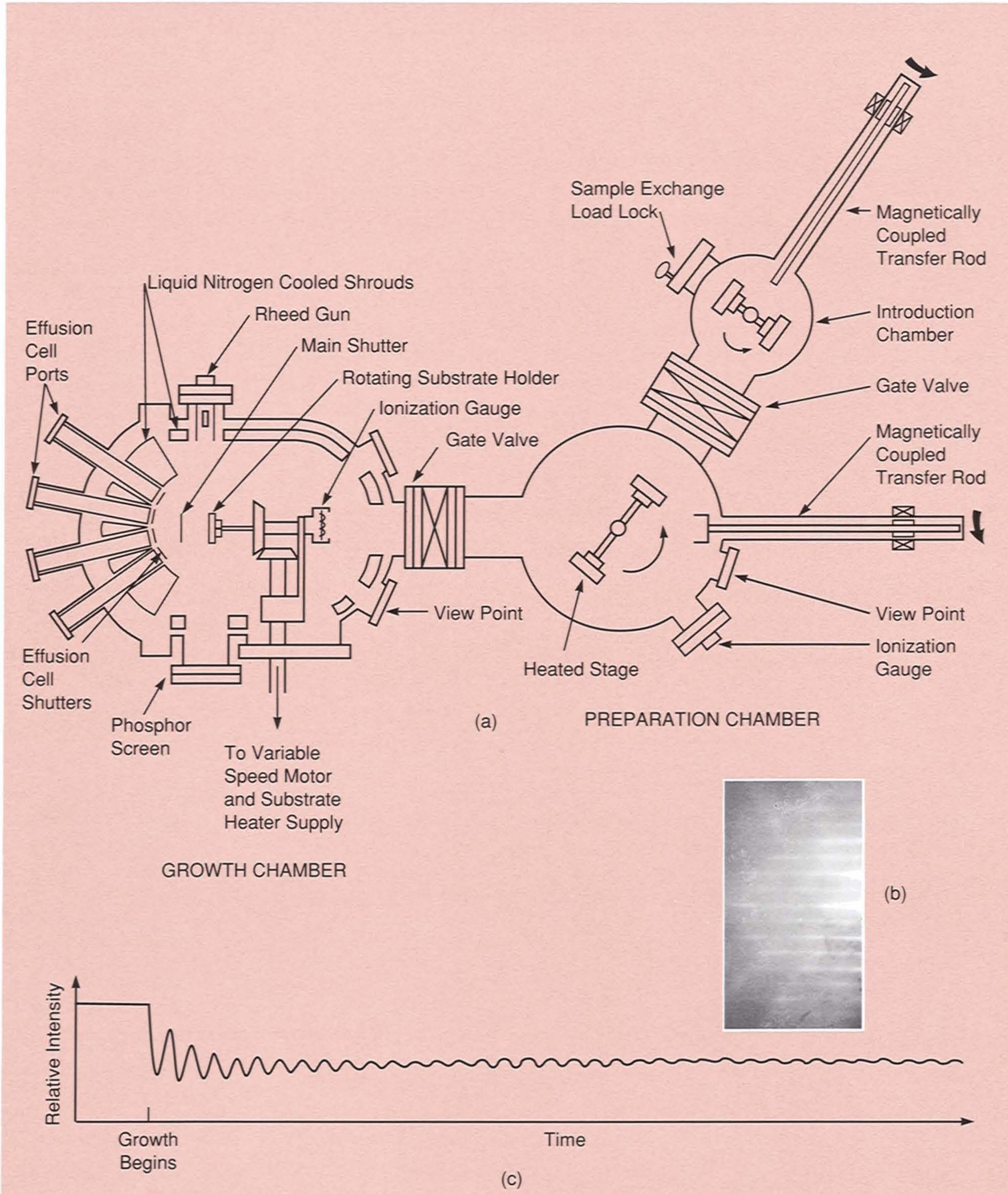

Fig. 8—(a) Diagram of an MBE system showing the relative position of the chambers, furnaces, cryopanels, substrate holding assembly, shutters, reflection electron-diffraction (RED) system, residual-gas analyzer, flux monitor, and molecular beams. (b) An arsenic-stabilized RED pattern. (c) A RED oscillation pattern.

micrometers, depending on the surface temperature and the type of element. In a steady-state situation, the rate at which Ga adatoms accumulate is equal to the difference of two rates: the rate at which Ga adatoms incorporate into a crystal, and the rate at which Ga adatoms evaporate from the surface. The relative rates of incorporation and desorption are controlled by the surface temperature and As flux density. As adatoms, on the other hand, will leave a hot surface almost instantaneously unless they are immediately bonded to Ga atoms. As a result, we control the GaAs growth rate by adjusting the Ga flux. At the same time, however, we also need to supply an As flux that delivers sufficient As to the growing surface to stabilize the desired surface reconstruction.

Figures 10(a), 10(b), and 10(c) are transmission-electron micrographs (TEM) of three structures, similar to those depicted in Fig. 4, of GaAs/$Al_xGa_{1-x}As$ materials grown with MBE. The layers that appear lighter in the micrographs contain more Al than the darker layers. The structure shown in Fig. 10(a) is only about 9.5 nm thick; it consists of two 2.5-nm-thick barriers and a 4.5-nm-thick quantum well. The structure of Fig. 10(a) is used to make high-speed resonant-tunneling oscillators [13]. The structure of Fig. 10(b) contains 100 quantum wells, which can be used as a light modulator [14, 15]. If the barrier thicknesses of this structure were reduced so that the well wave functions could couple, the structure would be called a superlattice. The structure of Fig. 10(c) contains a number of coupled quantum wells that we are studying for potential application as far-infrared radiation sources. As can be seen from the micrographs of Fig. 10, MBE is an excellent tool for fabricating structures with clean material interfaces and minuscule layer thicknesses.

In the remaining sections we will discuss several devices developed at Lincoln Laboratory. These devices exploit the optical-absorption and electron-transport properties of quantum-well technology.

Monolithic Integration of Lasers of Different Frequencies

Perhaps the most successful quantum-well device to date is the quantum-well laser [16], which utilizes the quantum properties of direct-gap materials to emit light. These lasers have been successfully grown by a variety of epitaxial-growth techniques. One version of the laser (Figs. 11[a], 11[b]) contains five square quantum wells embedded between two high Al-concentration cladding layers, which act as barriers. The cladding layers, one heavily doped p-type and the other heavily doped n-type, form a diode with a junction at the quantum wells. The structure is contained within an optical cavity that has two smooth mirrors at its opposing ends and contacts at its top and bottom (Fig. 11[c]).

As current is passed through the device, holes and electrons are injected into the quantum wells (Fig. 11[b]). The holes relax and are quantized into the lowest heavy-hole energy state. The electrons relax and are quantized into the lowest electron energy state. From these states, the electrons and holes recombine, emitting photons of energy $E_{hh} + E_{gap} + E_e$. The emitted light is guided by total internal reflection within the structure because the device's outer cladding layers have a lower index of refraction than the quantum-well structure. The difference in indices is due to the higher Al content of the outer cladding layers. (The higher bandgap of the cladding layers also helps to inject electrons and holes into the well region.) Because of the different indices of refraction of the materials involved, emitted light is guided and repeatedly reflected between the device's smooth, partially reflecting end mirrors, which form a Fabry-Perot cavity. The dynamics of the system generate stimulated emission, or lasing, in which the wavelength of the emitted light is directly related to the thickness of the quantum wells, through E_{hh} and E_e.

At Lincoln Laboratory, we used some of the unique properties of MBE to fabricate on a single surface reconstruction. We have observed that growing GaAs with a Ga-rich surface reconstruction, as in Fig. 9(a), usually leads to poor surface morphology. In the Ga-rich pattern of Fig. 9(a), the brighter and longer lines are related to the atomic planes of the bulk crystal. The three weaker lines between each pair of brighter lines are related to the crystal's surface reconstruction. In the Ga-stablilized pattern of Fig. 9(b), two weaker lines are visible between the bulk-crystal lines. In the As stabilized pattern of Fig. 9(c), one weaker line is visible between the bulk-crystal lines.

In addition, we can use the quality of a diffraction pattern as an indication of a layer's smoothness, since the long coherence length of the low-angle grazing-incidence electrons makes the pattern very sensitive to surface morphology, Spotty or dotted lines indicate a rough sample surface; sharp and continuous lines indicate a smooth sample surface.

We can also use RED to observe epitaxial growth monolayer by monolayer [12]. During crystal growth, the lines of a RED pattern oscillate in intensity before becoming steady state. Figure 8 shows such an intensity pattern as a function of time. The graph in Fig. 8(c) was generated by monitoring the intensity of a small portion of the primary line. We can associate each cycle in the line oscillation with the growth of a monolayer of crystal. The growth of a monolayer begins by the formation of small islands one monolayer thick that expand laterally as growth progresses until they coalesce into a single flat surface. Each of the lines, which represents a different order of diffraction, dims as that order is affected through scattering by the changing island sizes. The intensity of the lines is restored as the islands coalesce into a flat surface.

The dynamics of MBE crystal growth are worth noting. In a machine that uses elemental sources, the Ga beam contains primarily Ga atoms and the As beam contains As_4 molecules. After arriving onto a hot substrate surface, As_4 disassociates, and Ga and As surface adatoms are formed, i.e., atoms not yet incorporated into crystals. The adatoms can migrate for several

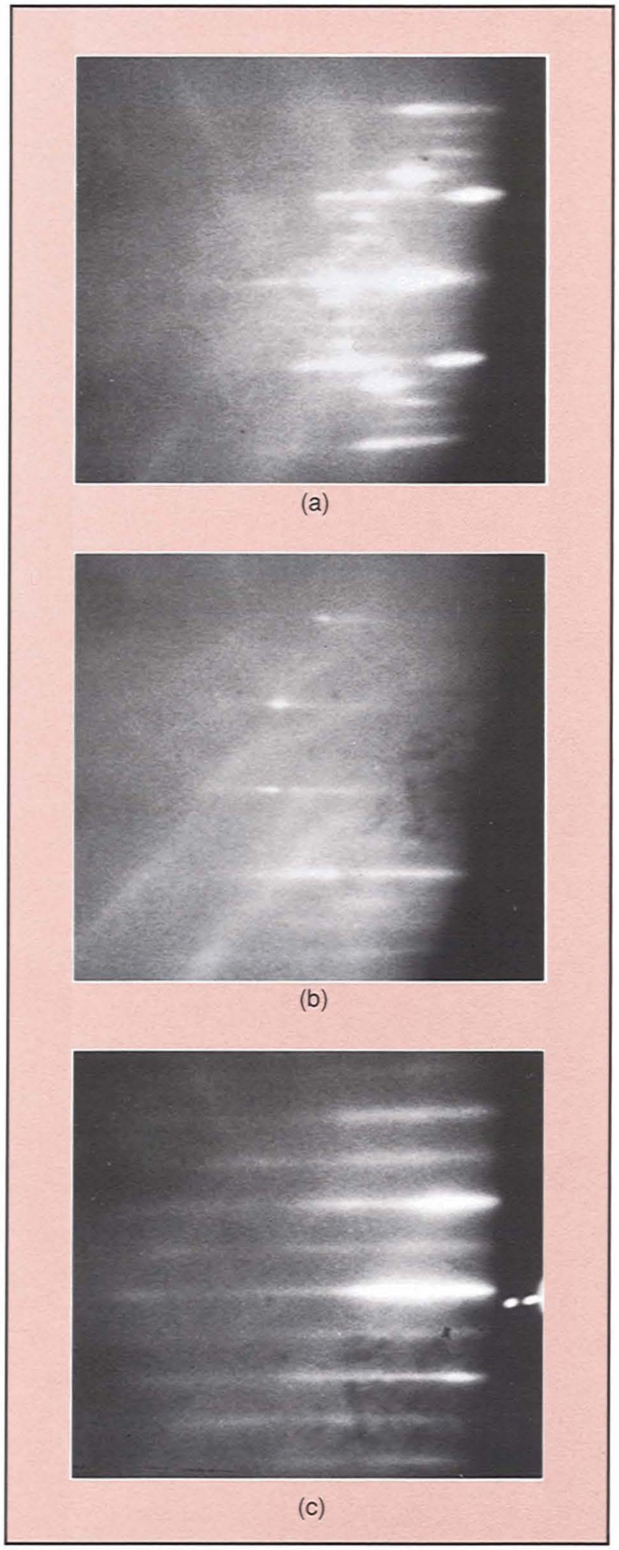

Fig. 9—RED patterns used to control growth dynamics on a GaAs surface. (a) Ga-rich pattern. (b) Ga-stabilized pattern. (c) As-stabilized pattern.

as the temperature increases. In addition, the loss of Ga in the AlGaAs layers causes an increase in the percentage of AlAs in the structure and a consequent increase in the barrier height of the AlGaAs layers. In the colder growth regions, in fact, this technique enables the growth of layers that behave as uncoupled quantum wells (Fig. 4[a]). In the hotter growth regions, the technique enables a continuous transition to a coupled or superlattice configuration (Fig. 4[e]).

To demonstrate that this technique could be used to integrate lasers of different wavelengths on one wafer, we grew the following epitaxial layers on a p-type GaAs substrate: a high-Al-content p-type AlGaAs cladding layer, a low-Al-content undoped AlGaAs layer, five GaAs active wells with undoped AlGaAs barriers, a low-Al-content undoped AlGaAs layer, a high-Al-content n-type AlGaAs cladding layer, and an n-type GaAs contacting layer. During the entire growth process, the substrate remained on a slotted MBE block. The slots were used to create zones of two different temperatures at the surface of the substrate. Figure 12 shows a cross section of the mounting block, the indium interface and vacuum slots, and the layer structure of the quantum-well lasers. When the temperature of the block was set at 710°C, the surface temperature was 710°C over the indium-contacted regions and 680°C over the uncontacted regions (in Fig. 12, the regions above the vacuums) as measured by a two-color infrared pyrometer. We timed the beam shutters to give nominal well and barrier thicknesses of 10 nm and 20 nm, respectively, at 680°C.

Figure 13 shows the intensity versus lasing wavelength, and the pulsed-power output versus current curves of typical lasers fabricated from the two regions of different temperatures of Fig. 12. Lasers from the colder region (Fig. 13[a]) had threshold currents of around 800 mA (resulting in threshold-current densities of around 0.9 kA/cm^2), differential quantum efficiencies of 15% per facet, and wavelengths around 865 nm. Lasers from the hotter region (Fig. 13[b]) had threshold currents of around 1,000 mA (corresponding to threshold-current densities of

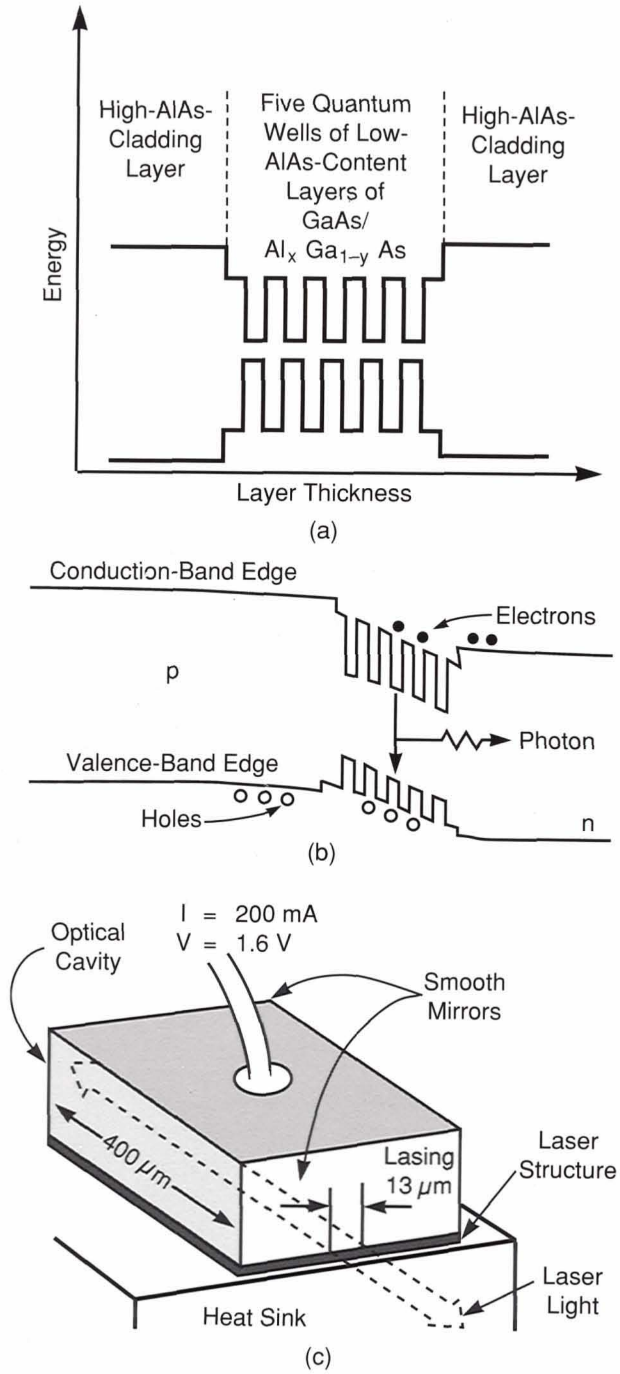

Fig. 11—A multiple-quantum-well (MQW) semiconductor diode laser. (a) The device's layered structure, which consists of high-AlAs-content cladding layers and a MQW structure of five wells of low-AlAs-content layers of GaAs/ $Al_xGa_{1-x}As$. (b) The structure under a forward bias. Electrons and holes are injected into the well structure where they relax into the lowest well states. The electrons and holes then recombine and the process results in photons being emitted. (c) The laser mounted on a heat sink.

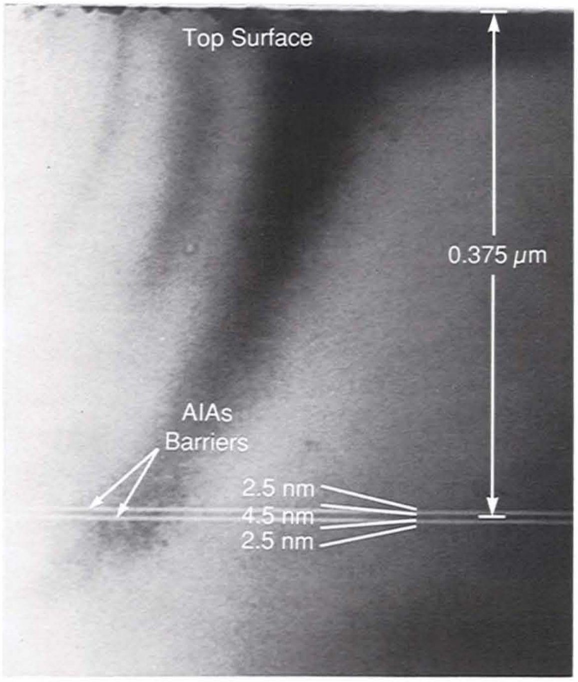

(a)

(b)

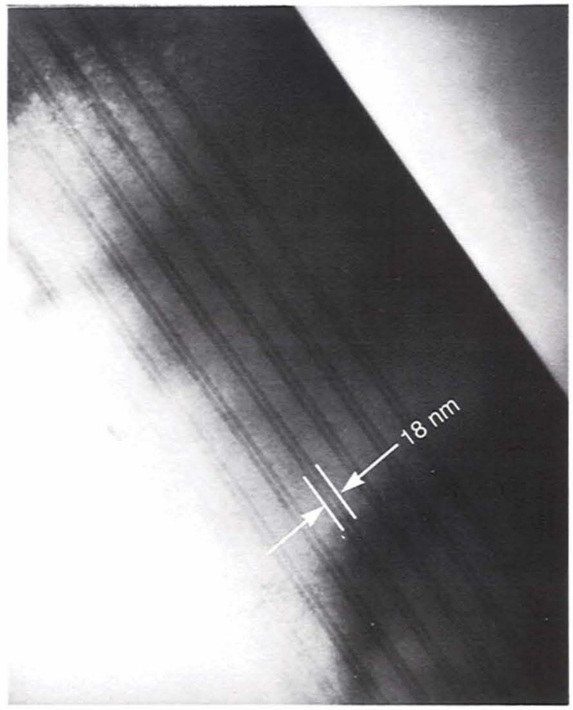

(c)

Fig. 10—Transmission electron micrographs of GaAs/AlGaAs structures grown with MBE. The micrograph in (a) shows a double-barrier structure similar to the one diagrammed in Fig. 4(c) The micrograph in (b) shows a number of GaAs/AlGaAs square quantum wells similar to the well diagrammed in Fig. 4(a) And the micrograph in (c) shows a number of symmetric coupled quantum wells, similar to those diagrammed in Fig. 4(d) but here symmetric rather than asymmetric.

wafer separate lasers that have similar structures (Fig. 11[a]) but operate at wavelengths that differ by as much as 40 nm. We achieved the wavelength difference by controlling the thicknesses of the quantum wells that form the active areas of the lasers. We controlled the thickness by manipulating the sticking coefficient of Ga—the ratio of the rate of Ga incorporation to the rate of Ga arrival at the surface of a wafer—through local variations of the substrate temperature during the growth process [17]. This technique could lead to a variety of important GaAs-based applications, such as the development of multiwavelength optical interconnects.

RED studies by groups at Cornell University [18] and the University of Minnesota [19] have indicated that the sticking coefficient of Ga dramatically decreases with substrate temperatures higher than 700°C. Therefore, in quantum-well structures grown above 700°C, the thickness of GaAs and AlGaAs layers decreases

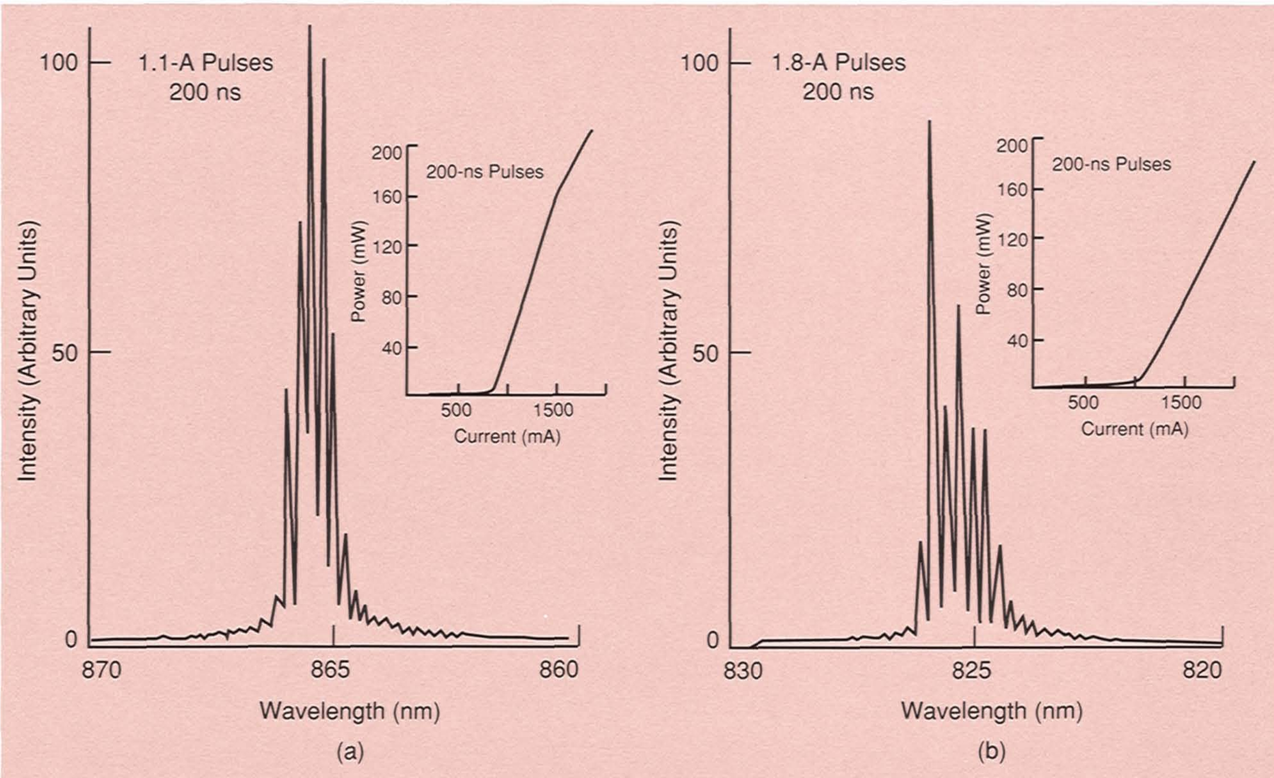

Fig. 13—Wavelength spectra and graphs of optical power versus current for lasers fabricated from both the colder (a) and hotter (b) regions of a wafer. As shown in the spectra, the difference in the wavelength of lasers fabricated from the two regions is about 40 nm.

the wave nature of electrons in a solid. The device's microwave and millimeter-wave applications were discussed in a previous *Lincoln Laboratory Journal* article [26].

In this article, we will show by example how the devices can be used to study basic materials and transport properties of quantum wells. The structures utilize thin AlAs barriers with thicknesses ranging from 11 to 30 Å and contain ohmic contacts above and below the active layers (Fig. 15[a]) [21]. Unless otherwise noted, the GaAs layers outside the double-barrier structure are n-type doped to about 1×10^{17} cm^{-3}.

Electrons tunnel through the thin barriers of a resonant-tunneling diode. We can use a qualitative optical model to analyze the structure in which we think of a resonant-tunneling diode as an electronic Fabry-Perot resonator. The two barriers of the diode are analogous to partially transmitting mirrors. The resonant-tunneling diode's electron transmission (i.e., the device's current) is a function of the device's incident electron energy (i.e., the device's voltage). As in an optical Fabry-Perot resonator, transmission peaks occur at the resonant energies of the cavity.

In order for the current-voltage (I-V) characteristic of a resonant-tunneling diode to have these peaks, the wave functions of the electrons must be coherent across the device's entire double-barrier structure. A variety of electron scattering events that occur in either the well or the barriers will destroy this coherence and, as a result, ruin the structure of the I-V characteristic.

We have used resonant-tunneling devices to understand how electrons in a GaAs quantum well interact with thin AlAs barriers. We have also investigated the maximum thicknesses that double-barrier structures can have before electron coherence is lost.

Figure 15(b) shows the room-temperature I-V characteristic of the double-barrier diode of Fig. 15(a). The two resonant peaks of the characteraround 1.5 kA/cm^2), differential quantum efficiencies of 7% per facet, and wavelengths around 825 nm. Figures 13(a) and 13(b) also show the wavelength spectra of the two types of lasers. We made no attempt to optimize the growth conditions with regard to threshold-current density.

A similar crystal-growing technique should enable the formation of at least three or four significantly different well thicknesses in regions of various sizes on the same wafer. Figure 14 shows a sketch of a 2 × 2 array of surface-emitting laser diodes, each with a different wavelength. In such arrays the emission from each element is reflected normal to the wafer surface by a built-in 45° reflecting mirror. At Lincoln Laboratory, we have developed a dry-etching technology that we have used successfully to fabricate such monolithic surface-emitting arrays of GaAs/AlGaAs diode lasers [20]. The array could be used as part of an interchip optical interconnect. Manipulation of the wafer from the back (e.g., by the inclusion of vacuums as in Fig. 12) or heating the wafer with focused radiation from the front could be used to control the thickness of the transition regions.

Resonant-Tunneling Diode

The resonant-tunneling diode is an interesting device because of its fundamental physics [21, 22] and applications [13, 23–25]. The device, which consists of a quantum well sandwiched between two thin barriers (Figs. 4[c] and 10[a]), provides a test structure that can improve our understanding of electron-transport properties perpendicular to a quantum well. The resonant-tunneling diode also demonstrates

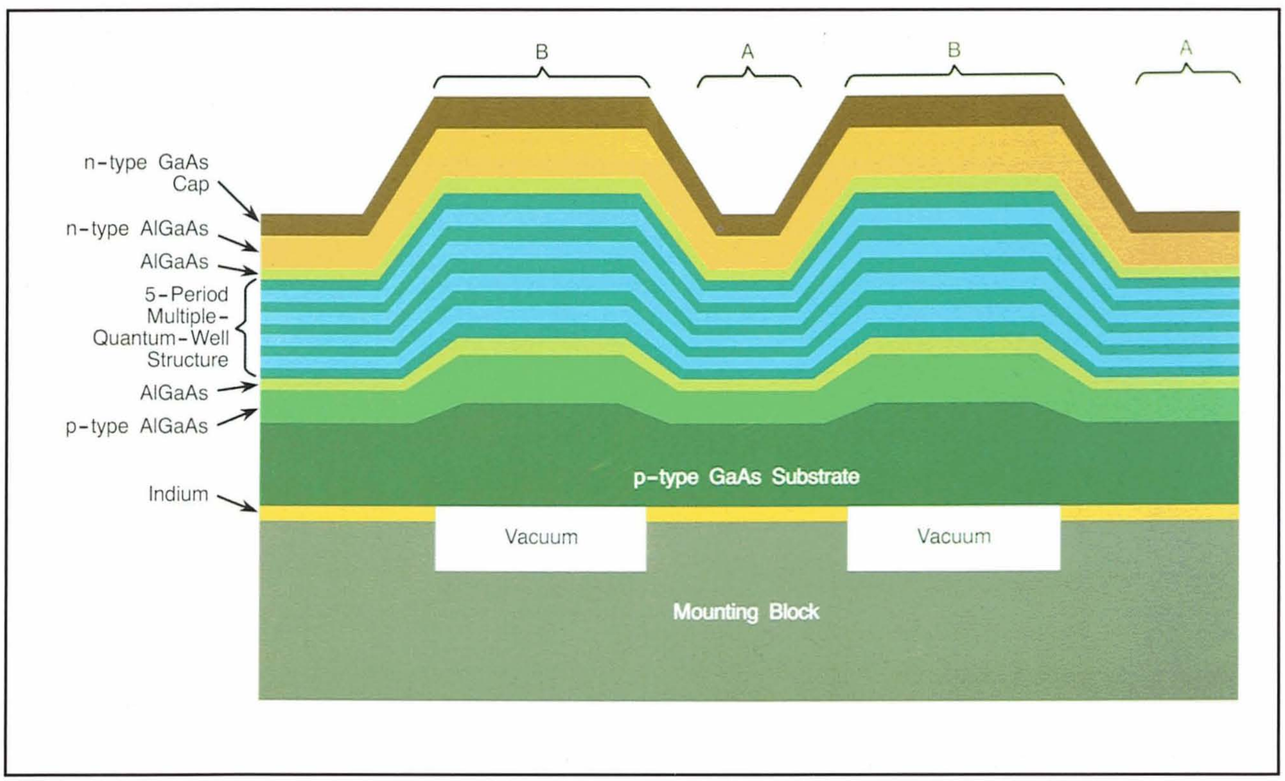

Fig. 12—Cross section of a slotted mounting block with a mounted wafer. The vertical scale has been exaggerated to give greater detail of the epitaxial layers, which form the laser structures. Note that in the hotter-surface-temperature regions, which are marked A, *the layers are thinner than in the colder-surface-temperature regions, which are marked* B.

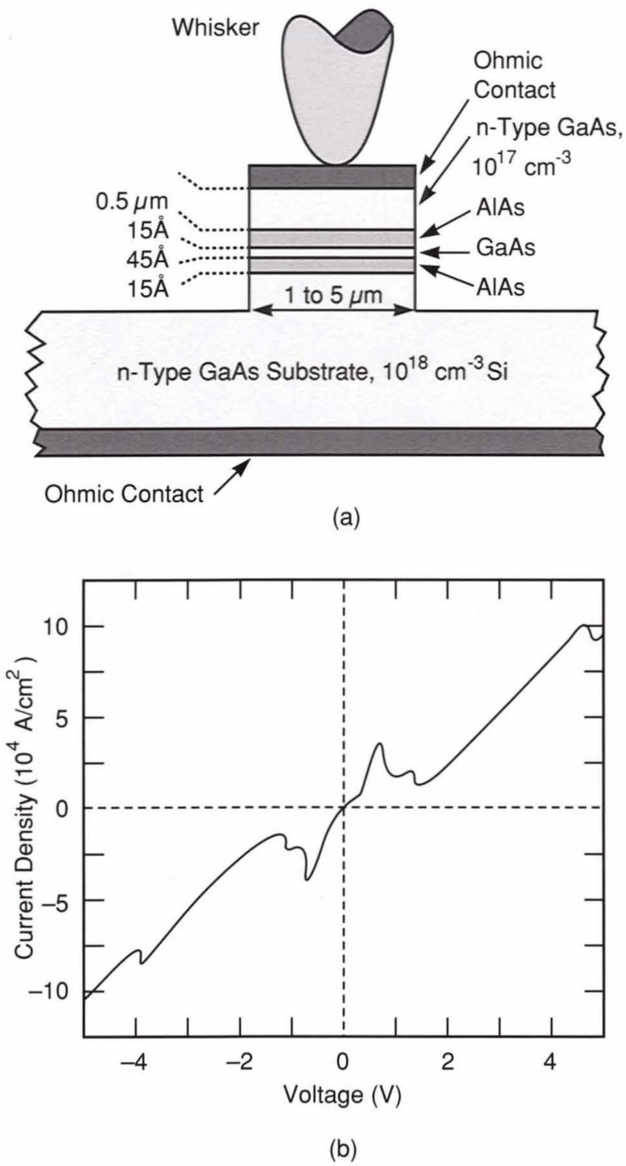

Fig. 15—Cross section (a) and I-V characteristic (b) of a double-barrier resonant-tunneling diode. For this particular device, the active thickness is about 75 Å and only two resonance states are possible. The states can be observed in the I-V characteristic as peaks at about 1.0 and 4.0 V at room temperature.

those dimensions to within 10% by using transmission-electron microscopy. All devices exhibited lower-voltage resonances at room temperature. At low temperatures, we observed a higher-voltage resonance as well. Because of the high current densities generated by the devices when they operate at the second, higher-voltage resonance, we obtained the I-V curves for these devices in a pulsed mode.

We used the resonant-tunneling theory described in Ref. 27 to determine the conduction-band discontinuity between GaAs and AlAs from these curves. Figure 16 shows one important result of this theory: in a resonant-tunneling diode, the position of the second resonance depends much more strongly on the structure's barrier height than does the position of the first resonance. (As it turns out, the position of the first resonance is related more to the structure's well thickness.) Consequently, we can estimate the height of a resonant-tunneling diode's barriers by noting the position of the diode's second resonance. Similarly, we can determine the thickness of the device's quantum well by noting the position of the first resonance.

When we investigated four samples—with barrier thicknesses between 15 and 25 Å, and well thicknesses between 45 and 56 Å—the best agreement with the theoretical I-V curves in each case required a conduction-band discontinuity of 1.0 ± 0.1 eV. In bulk AlAs, an indirect-gap material, the *X*-valley [5] of the conduction band is lower than the *Γ*-valley. The *X*-valley, therefore, determines the band edge of the material. By assuming that 65% of the bandgap discontinuity lies in the conduction band [28] and using the value of the *X*-valley band edge of bulk AlAs, we calculate the barrier height of bulk AlAs relative to GaAs to be 0.49 eV. On the other hand, by using the *Γ*-point energy gaps of 1.424 eV for GaAs and 3.018 eV for AlAs [29] and the 65% rule, we calculate the *Γ*-point discontinuity to be 1.036 eV. This result, which agrees with the value inferred from our measurement of 1.0 ± 0.1 eV, strongly suggests that direct *Γ*-valley tunneling processes are favored over indirect processes in a thin layer of AlAs.

The fact that thin AlAs barriers do not exhibit bulk properties is not surprising. The indirect processes of bulk materials require either phonon interactions (to conserve momentum) or other scattering processes (to allow for tunneling without momentum conservation). In thin AlAs barriers, however, few if any phonons can be created or absorbed because the time that an istic correspond to the two energy levels of the electron in the diode. The higher energy level is at about 0.62 eV and is over 0.1 eV higher than the predicted height of the AlAs barrier, if we assume the bulk band structure of AlAs in the calculation. This apparent experimental inconsistency indicates that using the bulk AlAs band structure, which is an indirect-gap semiconductor, may not be appropriate for analyzing ultrathin layers of AlAs. As we will see, thin AlAs barriers behave like direct-gap semiconductors. Therefore, we can use them with GaAs to produce barrier heights that are much larger than those predicted by using the band structure of bulk AlAs.

To determine the conduction-band discontinuity between AlAs and GaAs, we grew several double-barrier structures with barrier thicknesses between 15 and 25 Å and well thicknesses between 45 and 56 Å. We confirmed

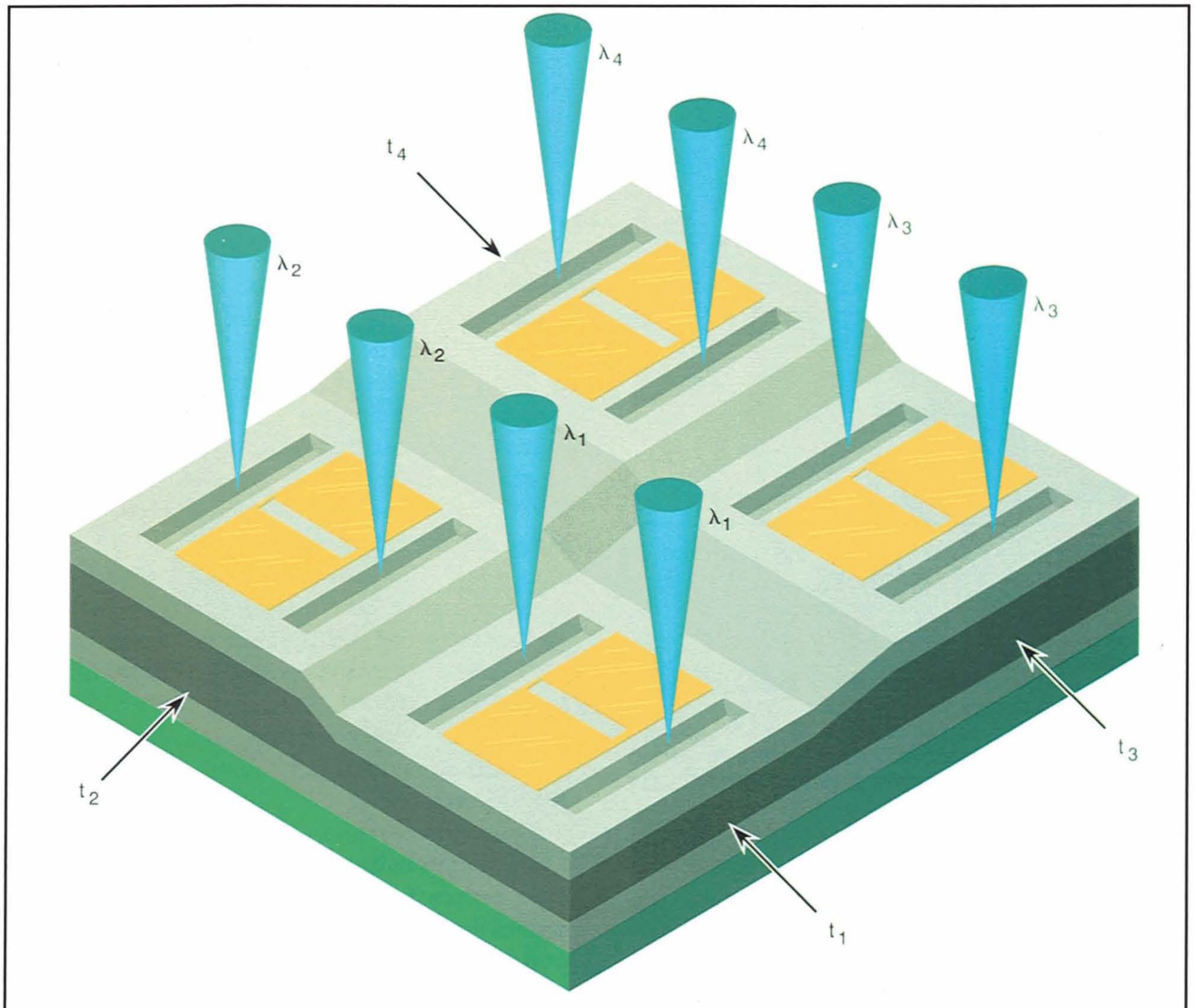

Fig. 14—Sketch of a 2 × 2 array of surface-emitting laser diodes. Through the use of the thickness-variation process, each laser operates at a different wavelength.

able to keep up with the incoming data stream. All of the above devices can be implemented with QWCCDs.

In the QWCCD we have placed the dopant in the top AlGaAs barrier close to the quantum-well channel. To minimize energy the dopant electrons ionize and collect in the channel. The QWCCD, therefore, is fundamentally different from other devices—such as conventional Schottky-barrier field-effect transistors (FET) and buried-channel CCDs—in which electron carriers and dopant atoms share the same regions. The absence of dopant atoms from the channel region reduces impurity scattering and increases the carrier mobility of the region.

Although high carrier mobility is desirable, the

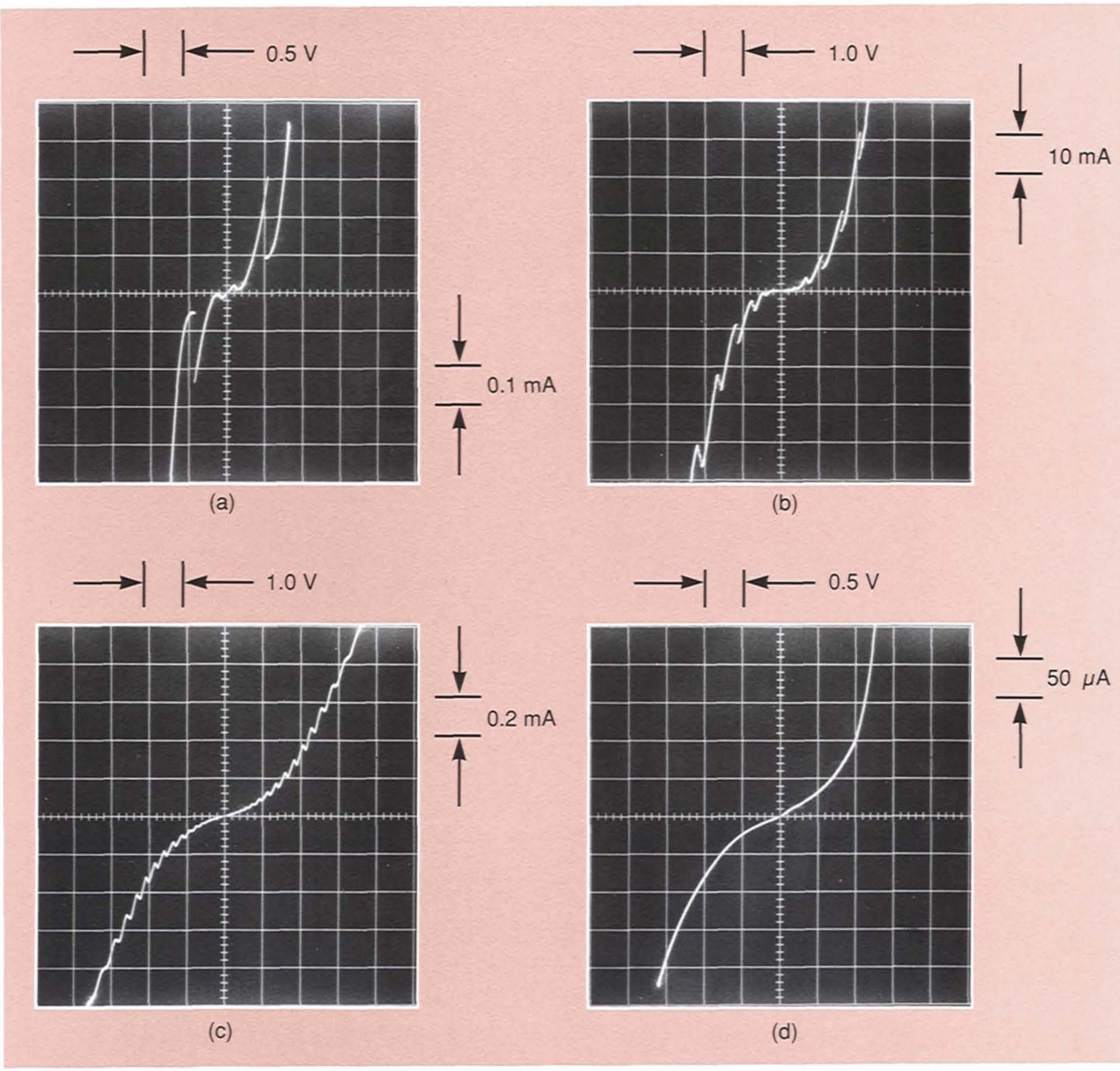

Fig. 17—I-V characteristics for a set of double-barrier structures with well thicknesses of (a) 10 nm, (b) 25 nm, (c) 50 nm, and (d) 100 nm at 77 K. Note that the number of steps in the I-V characteristic increases as the well thickness increases. Each step corresponds to an energy level in the well.

electron wave packet spends within the structure is prohibitively short. Nonetheless, impurity-assisted, or crystal-defect-assisted, tunneling is certainly present in thin AlAs barriers. We believe that this type of tunneling is responsible for the rapidly increasing currents in the second resonance region.

Electrons can remain coherent in double-barrier structures for relatively long distances. Figures 17(a) through 17(d) show the I-V characteristics at 77 K of wells that are respectively 10, 25, 50, and 100 nm thick. Remarkably, evidence of peaks, which correspond to the different energy states in a well, are clearly visible with thicknesses up to 50 nm. For greater thicknesses, the different energy states become so close together that the structure must be cooled to liquid-helium temperatures in order to prevent thermal effects from washing out the peaks. By analyzing a number of resonant-tunneling diodes of different well thicknesses, we found that the peaks are lost at around 100 nm. This observation implies that the coherence length of electrons in GaAs is about 100 nm.

We are also using resonant-tunneling diodes to investigate a variety of phenomena such as intervalley scattering and ballistic transport in GaAs. By studying resonant-tunneling diodes, we eventually hope to understand electron transport in more complicated, multiperiod superlattices.

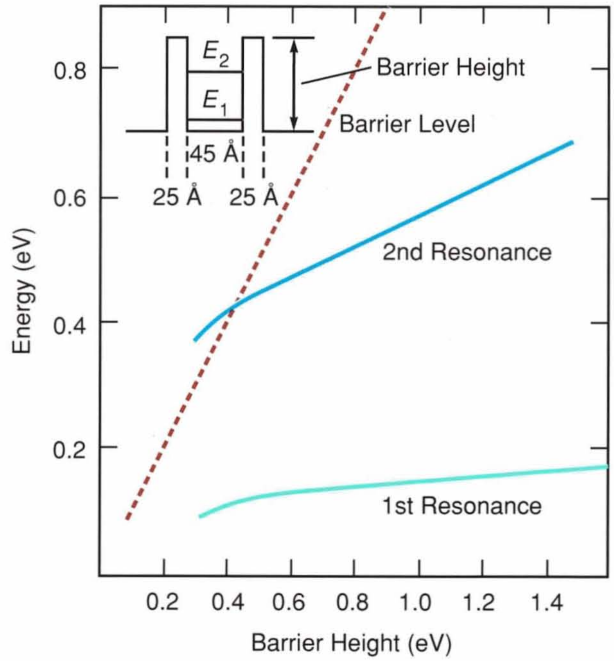

Fig. 16—Energy versus barrier height for a double-barrier resonant-tunneling diode. Note that the second resonance is much more sensitive to barrier-height differences than the first resonance.

Quantum-Well Charge-Coupled Device

In quantum-well charge-coupled devices (QWCCD), packets of electrons are clocked through a quantum-well channel with a series of charge-controlling gates [30]. QWCCDs are useful as imagers [31], for dynamic storage [32], and as control elements [14, 15].

Charge-coupled devices (CCDs) have one common feature: the ability to move packets of electrons from one position to another in an epitaxial layer without losing any electrons. The CCD in an imager is composed of a channel layer above which lies a two-dimensional array of semitransparent gates. If we apply the appropriate electrical bias to the gates, images projected onto the device will generate electrons in the channel layer that have local densities proportional to the local intensities of the images. If we then bias the gates sequentially, the electrons under each gate are collected into packets and sequentially swept to an output electrode. This process results in a video signal from which the image can be reconstructed. Another application of CCDs is in electronic systems, such as radars, that need to receive short bursts of data at high repetition rates. As a result, quick dynamic storage of incoming data is necessary. By using a bank of CCDs as a fast buffer memory we can store each data burst as a number of electron packets in one of the CCDs. The electron packets can then be transferred, at a slower rate, to a microprocessor. For example, if a microprocessor is able to process only one burst of data in the time that eight bursts are received, a system consisting of a bank of eight CCDs with eight parallel microprocessors would be

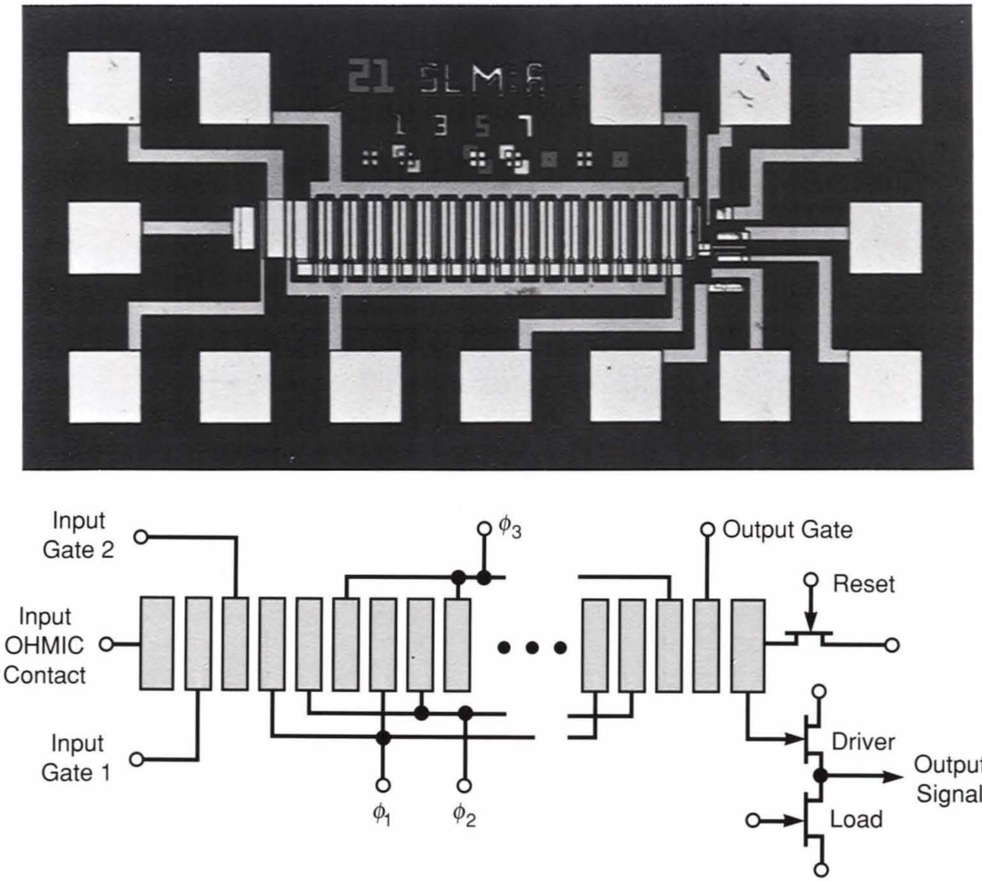

Fig. 19—Photograph and schematic of a 16-stage QWCCD. The output circuit consists of quantum-well high-electron mobility transistors (HEMT).

The purpose of the GaAs cap layer was for ohmic-contact formation; we etched the layer off the noncontact areas of the QWCCDs. We used an AlAs mole fraction of 0.30 in all of the AlGaAs layers, and we grew all of the layers at a temperature of 715°C.

Figure 19 shows a photograph and schematic of a three-phase, 16-stage QWCCD. We formed the Schottky-barrier gates in a single layer of Ti/Au. Each of the gates is 10 μm long with interelectrode gaps of about 1 μm between the gates. The electron packets are therefore controlled along a 176-μm-long channel. We achieved channel isolation through the use of proton implantation. Three quantum-well FETs form the output charge-detection circuit and have the same channel and gate material as the CCD. Because the gate length of the driver

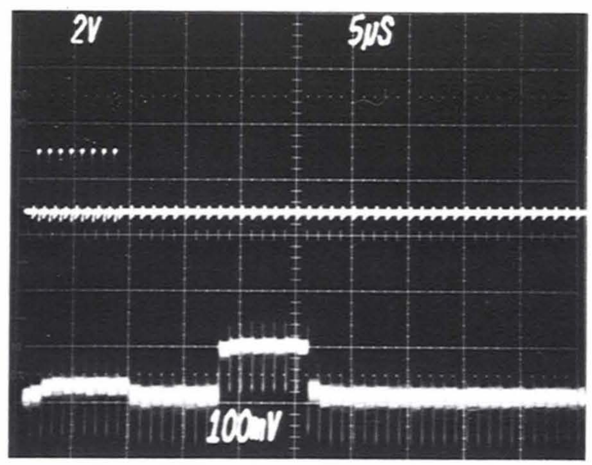

Fig. 20—Electrical performance of a QWCCD at a 1-MHz clock rate. The upper trace is the input signal to the device and the lower trace is the delayed output. A small amount of direct coupling of the input can be seen in the lower trace.

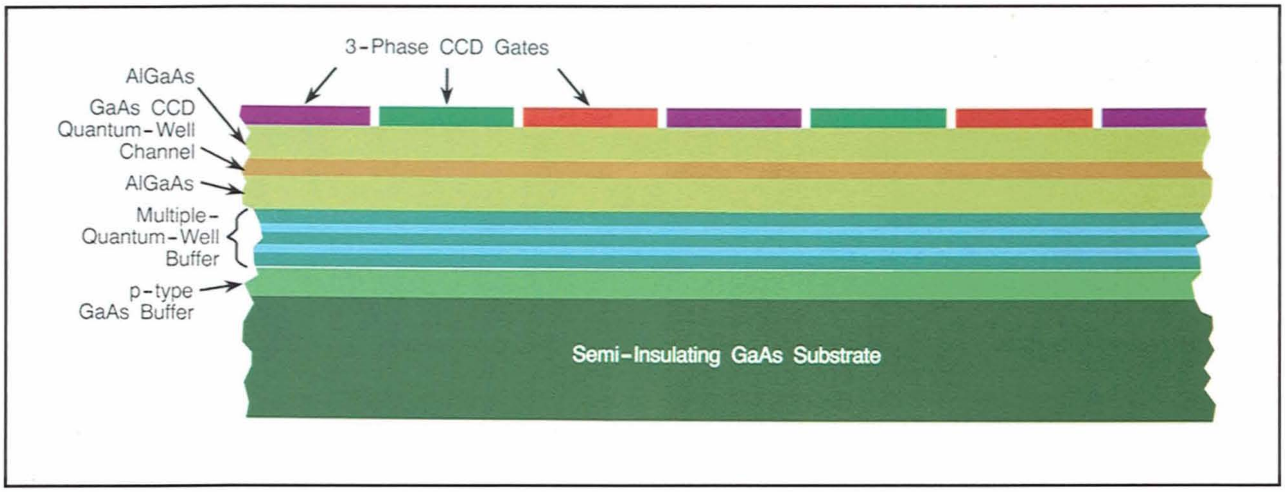

Fig. 18—Cross section of a portion of a quantum-well charge-coupled device (QWCCD) showing the three-phase gate structure, the GaAs quantum-well channel, and electron packets in the channel.

principal virtue of quantum confinement in a CCD is that the confinement minimizes the volume of electron packets. If electron-packet volumes are kept small, we can avoid bulk trapping and, as a result, maintain good charge-transfer efficiencies.

We have designed a QWCCD so that its electron packets affect the electric field passing through the device's underlying epitaxial layers. An example of a QWCCD that utilizes this effect is the CCD-addressed spatial light modulator [14, 15]. In such a device, we grow the epitaxial layers to form a multiple-quantum-well (MQW) structure before the channel layer is grown. The peak absorption of light passing through the structure changes as a function of the electric field applied across the MQW structure. Thus, we can modulate the intensity of light passing through the device by using the CCD's two-dimensional electron packets as local-field control elements. Such two-dimensional modulators are useful for optical processing applications.

A schematic illustration of such a QWCCD is shown in Fig. 18. We formed the quantum-well channel by sandwiching a 10-to-20-nm-thick undoped layer of GaAs between two layers of $Al_xGa_{1-x}As$. The lower AlGaAs layer was not doped and the upper layer was doped n-type. The upper layer supplies the space charge needed to establish the electric fields within the device. As discussed earlier, the conduction band in GaAs is approximately 200 meV lower than in the adjacent AlGaAs layers. This energy difference confines the electron packets within the CCD channel.

Figure 18 also illustrates the gate structure of a CCD. The gates, which establish the driving potentials for defining and transporting electron packets, must form good Schottky barriers to the underlying AlGaAs layer. We can thus fabricate CCD gates and channels on the same substrates as the quantum-well FETs. In such circuits, the enhanced electron mobility in the quantum-well channel is an important benefit.

Our structure consisted (from bottom to top) of a

semi-insulating GaAs substrate,
1.0-μm-thick buffer layer of p-type GaAs,
2.0-μm-thick superlattice buffer layer of GaAs/AlGaAs,
40-nm-thick isolation layer of AlGaAs,
14-nm-thick undoped QWCCD channel,
4.0-nm-thick isolation layer of undoped AlGaAs,
100-nm-thick layer of n-type AlGaAs (doped to 2×10^{17} cm^{-3}), and
cap of n-type GaAs.

Auger analysis. A special note of thanks is due to H.Q. Le, A.R. Calawa, R.A. Murphy, I. Melngailis, and A.L. McWhorter for their helpful comments and proofreading of this article.

Portions of this work were sponsored by the Department of the Air Force, DARPA, the Department of the Navy for SDIO, the U.S. Army Research Office, and NASA.

quantum-well FET is 5 μm, the circuit cannot take full advantage of the high-bandwidth capability of this type of FET. The threshold voltage of the FETs and of the CCD channel is about -1.0 V.

An example of the electrical performance of this device at a clock rate of 1.0 MHz is shown in Fig. 20. The upper trace of the figure shows the input, a sequence of eight pulses, to the device, and the lower trace shows the delayed output. The electron-packet density in the channel is around 10^{10} cm^{-2}. (Because of the minuscule thicknesses of channels, a channel's density, called *sheet density*, is measured in terms of the channel's other two dimensions.)

In the delayed-output curve of Fig. 20, the slightly lower amplitude of the first pulse is due to charge-transfer inefficiency in which a fractional charge loss per stage of about 0.17% occurs. We believe that the transfer inefficiency is due to the presence of potential gaps that form beneath the interelectrode gaps [33] rather than to the quality of the fabricated materials. We can eliminate this problem by reducing the gap size, and we are currently investigating the use of an overlapping-gate scheme, which would enable us to have better control over the gap dimensions [34].

Measurements of bulk-trapping effects in a CCD are usually made by sending bursts of electron packets through the device every t seconds. During the time interval t, bulk traps in the CCD release their charges into empty quantum wells, and the next burst of electron packets passing through the device refills the traps. Consequently, the charge loss of the packets is related to the number of traps emptied during time t.

In preliminary measurements, we used values of t from 1 μs to 20 ms and observed no increase in charge loss. Our results indicate that the trap-sheet density is $<10^{10}$ cm^{-2} for traps with emission times between 1 μs and 20 ms, and that the electrons were completely confined in the GaAs quantum wells. The extension of t beyond our initial range of 1 μs to 20 ms could be useful in studying traps in superlattice structures.

Summary

In this article, we have discussed the basic phenomena of quantum-well device engineering and MBE. The combined technology has been used to fabricate successfully a number of quantum-well devices from semiconductor materials with synthetic, or custom-designed, bandgaps. Examples of devices that utilized optical and transport properties of quantum wells were discussed. Although this article concentrated on MBE, other techniques such as metal-organic vapor deposition [35] and atomic-layer epitaxy [36] have also been used successfully in quantum-well-device engineering.

This article focused on the GaAs/AlGaAs materials system. However, many other materials systems will support the fundamentally quantum-mechanical behavior described here. We are rapidly approaching the point where we will be able to fabricate specific materials with properties optimized for given desired electrical or optical functions. Finally, this article showed that by studying quantum wells we can gain important information about the properties of electrons in crystalline semiconductor materials.

Acknowledgments

The work described in this article was performed by several teams at Lincoln Laboratory. The MBE team included A.R. Calawa, S.J. Eglash, M.J. Manfra, J.V. Pantano, F.W. Smith, and G.W. Turner. The team of R.J. Bailey, J.P. Donnelly, R.C. Hancock, G.D. Johnson, and J.J. Zayhowski worked on monolithic multifrequency laser arrays. The resonant-tunneling team included J.W. Bales, E.R. Brown, A.R. Calawa, C.L. Chen, G.D. Johnson, H.Q. Le, L.J. Mahoney, M.J. Manfra, K.A. McIntosh, K.M. Molvar, C.D. Parker, and T.C.L.G. Sollner. The GaAs/AlGaAs CCD team consisted of B.F. Aull, B.E. Burke, B.F. Gramstorff, G.D. Johnson, and K.B. Nichols.

The author also wishes to acknowledge the mask-making and contact-metallization teams of the Laboratory's Group 87, G.D. Johnson for TEM sample preparation, and M.C. Finn for

WILLIAM D. GOODHUE is a staff member in the Microelectronics Group. His research interests include quantum-well-device physics, device fabrication, and molecular-beam epitaxy. Bill has worked at Lincoln Laboratory in a number of capacities over the last 11 years. Before rejoining Lincoln Laboratory five years ago, Bill worked for the United Technologies Research Center. He received a B.S. in mathematics from Worcester Polytech Institute, an M.A. in mathematics from the University of Massachusetts in Amherst, and a Ph.D. in physics from the University of Lowell. In his spare time, Bill enjoys hiking and fishing with his family.

References

1. R. Dingle, "Confined Carrier Quantum States in Ultrathin Semiconductor Heterostructures," *Festkörper Probleme XV: Advances in Solid State Physics* (Pergamon, New York, 1975), pp. 21–28.
2. A.Y. Cho, "Growth of III-V Semiconductors by Molecular-Beam Epitaxy and Their Properties," *Thin Solid Films* **100**, 291 (1983).
3. L. Esaki, "A Bird's-Eye View on the Evolution of Semiconductor Superlattices and Quantum Wells," *IEEE J. Quantum Electron.* **QE-22,** 1611 (1986).
4. C. Kittel, *Introduction to Solid State Physics*, 4th ed. (John Wiley, New York, 1971).
5. S.M. Sze, *Physics of Semiconductor Devices*, 2nd ed. (John Wiley, New York, 1981).
6. F.K. Richtmyer, E.H. Kennard, and J.N. Cooper, *Introduction to Modern Physics*, 6th ed. (McGraw-Hill, New York, 1969).
7. H.Q. Le, J.J. Zayhowski, and W.D. Goodhue, "Stark Effect in $Al_xGa_{1-x}As$/GaAs Coupled Quantum Wells," *Appl. Phys. Lett.* **50**, 1518 (1987).
8. H.Q. Le, J.V. Hryniewicz, W.D. Goodhue, and V.A. Mims, "Optical Nonlinearities in $Al_xGa_{1-x}As$/GaAs Asymmetric Coupled Quantum Wells," *Optics Lett.* **13**, 859 (1988).
9. A.Y. Cho and J.R. Arthur, "Molecular-Beam Epitaxy," *Prog. Solid State Chem.* **10**, 157 (1975).
10. L. Esaki and R. Tsu, "Superlattice and Negative Conductivity in Semiconductors," *IBM Res. Note*, RC-2418 (1969).
11. L.L. Chang, L. Esaki, and R. Tsu, "Resonant Tunneling in Semiconductor Double Barriers," *Appl. Phys. Lett.* **24**, 593 (1974).
12. J.M. Van Hove, C.S. Lent, P.R. Pukite, and P.I. Cohen, "Damped Oscillations in Reflection High Energy Electron Diffraction during GaAs MBE," *J. Vac. Sci. Technol. B* **1**, 741 (1983).
13. E.R. Brown, W.D. Goodhue, and T.C.L.G. Sollner, "Fundamental Oscillations up to 200 GHz in Resonant Tunneling Diodes and New Estimates of Their Maximum Oscillation Frequency from Stationary-State Tunneling Theory," *J. Appl. Phys.* **64**, 1519 (1988).
14. K.B. Nichols, B.E. Burke, B.F. Aull, W.D. Goodhue, B.F. Gramstorff, C.D. Hoyt, and A. Vera, "Spatial Light Modulators Using Charge-Coupled–Device Addressing and Electroabsorption Effects in GaAs/AlGaAs Multiple Quantum Wells," *Appl. Phys. Lett.* **52**, 1116 (1988).
15. W.D. Goodhue, B.E. Burke, B.F. Aull, and K.B. Nichols, "Molecular Beam Epitaxially Grown Spatial Light Modulators with Charge-Coupled–Device Addressing," *J. Vac. Sci. Technol. A* **6**, 2356 (1988).
16. N. Holonyak, Jr., "Quantum-Well Semiconductor Lasers," *Sov. Phys. Semicond.* **19**, 943 (1985).
17. W.D. Goodhue, J.J. Zayhowski, and K.B. Nichols, "Planar Quantum Wells with Spatially Dependent Thicknesses and Al Content," *J. Vac. Sci. Technol. B* **6**, 846 (1988).
18. J. Ralston, G.W. Wicks, and L.F. Eastman, "Reflection High-Energy Electron Diffraction Intensity Oscillation Study of Ga Desorption from Molecular Beam Epitaxially Grown $Al_xGa_{1-x}As$," *J. Vac. Sci. Technol. B* **4**, 594 (1986).
19. J.M. Van Hove, P.R. Pukite, G.J. Whaley, A.M. Wowchak, and P.I. Cohen, "Summary Abstract: Layer-by-Layer Evaporation of GaAs (001)," *J. Vac. Sci. Technol. B* **3**, 1116 (1985).
20. J.P. Donnelly, W.D. Goodhue, T.H. Windhorn, and R.J. Bailey, "Monolithic Two-Dimensional Surface-Emitting Arrays of GaAs/AlGaAs Diode Lasers," *Appl. Phys. Lett.* **51**, 1138 (1987).
21. W.D. Goodhue, T.C.L.G. Sollner, H.Q. Le, E.R. Brown, and B.A. Vojak, "Large Room-Temperature Effects from Resonant Tunneling through AlAs Barriers," *Appl. Phys. Lett.* **49**, 1086 (1986).
22. E.R. Brown and W.D. Goodhue, "A New Method to Detect Ballistic Electrons in GaAs," *Proc. IEEE/Cornell Conf. on Advanced Concepts in High Speed Semiconductor Devices and Circuits, Cornell University, Ithaca, NY, 10–12 Aug. 1987*, p. 326.
23. T.C.L.G. Sollner, W.D. Goodhue, P.E. Tannenwald, C.D. Parker, and D.D. Peck, "Resonant Tunneling through Quantum Wells at Frequencies up to 2.5 THz," *Appl. Phys. Lett.* **43**, 588 (1983).
24. T.C.L.G. Sollner, P.E. Tannenwald, D.D. Peck, and W.D. Goodhue, "Quantum Well Oscillators," *Appl. Phys. Lett.* **45**, 1319 (1984).
25. N. Yokoyama, K. Imamura, T. Ohshima, H. Nishi, S. Muto, K. Kondo, and S. Hiyamizu, "Tunneling Hot Electron Transistor Using GaAs/AlGaAs Heterojunctions," *Jpn. J. Appl. Phys.* **23**, L311 (1984).
26. T.C.L.G. Sollner, E.R. Brown, and H.Q. Le, "Microwave and Millimeter-Wave Resonant-Tunneling Devices," *Lincoln Laboratory Journal* **1**, 89 (1988).
27. T.C.L.J. Sollner, H.Q. Le, C.A. Correa, and W.D. Goodhue, "Persistent Photoconductivity in Quantum Well Resonators," *Appl. Phys. Lett.* **47**, 36 (1985).
28. D. Arnold, A Ketterson, T. Henderson, J. Klem, and H. Morkoç, "Determination of the Valence-Band Discontinuity between GaAs and (Al, Ga)As by the Use of p^+-GaAs-(Al, Ga)As-p^--GaAs Capacitors," *Appl. Phys. Lett.* **45**, 1237 (1984).
29. H.C. Casey and M.B. Panish, *Heterostructure Lasers, Part A: Fundamental Principles* (Academic Press, New York, 1978), p. 193.
30. W.D. Goodhue, B.E. Burke, K.B. Nichols, G.M. Metze, and G.D. Johnson, "Quantum-Well Charge-Coupled Devices for Charge-Coupled Device-Addressed Multiple-Quantum-Well Spatial Light Modulators," *J. Vac. Sci. Technol. B* **4**, 769 (1986).
31. B.E. Burke, R.W. Mountain, P.J. Daniels, and D.C. Harrison, "420 × 420 Charge-Coupled-Device Imager and Four-Chip Hybrid Focal Plane," *Opt. Eng.* **26**, 890 (1987).
32. D.L. Smythe, R.W. Ralston, B.E. Burke, and E. Stern, "An Acoustic SAW/CCD Buffer Memory Device," *Appl. Phys. Lett.* **33**, 1025 (1978).
33. I. Deyhimy, R.C. Eden, and J.S. Harris, "GaAs and Related Heterojunction Charge-Coupled Devices," *IEEE Trans. Electron Devices* **ED-27**, 1172 (1980).
34. K.B. Nichols and B.E. Burke, "A Gallium Arsenide Overlapping-Gate Charge-Coupled Device," *IEEE Electron Device Lett.* **EDL-6**, 237 (1985).
35. P.D. Dapkus "Metal-Organic Chemical Vapor Deposition," *Annu. Rev. Mater. Sci.* **12**, 243 (1982).
36. S.M. Bedair, M.A. Tischler, T. Katsuyama, and N.A. El-Masry, "Atomic Layer Epitaxy of III-V Binary Compounds," *Appl. Phys. Lett.* **47**, 51 (1985).